



Microstructure, Nanoindentation and Corrosion Behavior of Colmonoy-5 Deposition on SS410 Substrate Using Laser Cladding Process

Sundara Subramanian Karuppasamy¹ · N. Jeyaprakash^{1,2} · Che-Hua Yang^{1,2}

Received: 15 August 2021 / Accepted: 8 November 2021 / Published online: 6 January 2022
© King Fahd University of Petroleum & Minerals 2021

Abstract

Stainless steel 410 (SS410) is majorly used in manufacturing the components of gas turbines, pump shafts, thermal power plants, safety valves, and reactor core components that operate in severe aggressive environments. Prolonged exposure of these critical components in such environments results in reduction in their mechanical properties like tensile strength, hardness, wear, and corrosion resistance thereby causing failures and property losses. The present study is aimed to enhance the corrosion resistance behavior of SS410 by depositing the Colmonoy-5 alloy particles by means of laser cladding technique. The microstructure and hardness studies were carried out to reveal the formation of structure and improvement in hardness, respectively. Further, the corrosion analysis was performed on both the base and cladded samples in different duration with the test solution made from 3.5 wt% NaCl. Then, the corroded surface morphology and their corresponding roughness were analyzed. The results showed that the existence of the floret-shaped structure was observed on the cladded surface and improved the hardness due to the presence of chromium borides and carbides in the γ -nickel matrix. Among the various duration, the 8 h cladded sample exhibits high resistance to corrosion due to the formation of finite passivation film made by Cr-rich borides. In addition to that, the reduced surface roughness was observed on the 8 h cladded sample when compared with the base and other clad samples.

Keywords SS410 substrate · Colmonoy-5 cladding · Nano hardness · Vickers microhardness · Corrosion mechanism · Surface roughness

Abbreviations

SS410	Stainless steel 410
PVD	Physical vapor deposition
HVOF	High-velocity oxygen fuel
FESEM	Field emission scanning electron microscope
EDS	Energy-dispersive X-ray spectroscopy

Yb: YAG	Ytterbium-doped yttrium aluminum garnet
EIS	Electrochemical impedance spectroscopy (EIS)
R_p	Polarization resistance
R_s	Solution resistance
CPE	Constant phase element
SPM	Scanning probe microscopy

✉ N. Jeyaprakash
prakash84gct@gmail.com; prakash@ntut.edu.tw

Sundara Subramanian Karuppasamy
diwaha3@gmail.com

Che-Hua Yang
chyang@ntut.edu.tw

¹ Graduate Institute of Manufacturing Technology, National Taipei University of Technology, Taipei 10608, Taiwan, ROC

² Additive Manufacturing Center for Mass Customization Production, National Taipei University of Technology, Taipei 10608, Taiwan, ROC

1 Introduction

Stainless steel 410 (SS410) is the most preferred material for manufacturing jet engine parts, shafts, valves, storage tanks, gas, and steam turbines. This grade has a greater hardness, higher tensile strength, good wear resistance, excellent creep and fatigue strength which make it get implemented in severe aggressive environments [1, 2]. Conversely, long time exposure of this steel in such environment causes corrosion, which may lead to cataclysmic failure of those components, followed by loss of property, and in severe cases, it may



result in disaster. Generally, hydraulic turbines which operate in chloride environments are prone to initiation of pitting. This pitting initiation lowers the corrosion resistance due to the existence of preferential sites of undissolved chromium-rich phases [3]. The development of pitting initiation at the circumference of these chromium phases plays a vital role in promoting the breakage of the formed oxide film on the material [4]. In high-temperature usage, the Cl^- ions facilitate the thermoplastic decomposition of the film thereby decreasing the lifetime of the components [5]. In some cases, the presence of H_2S in oil wells expedites the corrosion rate of SS410 tubes at low temperatures [6]. Factors like chloride environment, high temperature, and acid containments greatly influence the corrosion resistance of SS410. Since the corrosion takes place at the surface level, to improve the resistance and service life of the components, several surface engineering techniques were currently practiced to improve the durability of the components. Physical Vapor Deposition (PVD) is one of the surface engineering techniques where the PVD treated surface exhibits finite grain structure and also it is easy to analyze the tribological properties on the treated surface. The major drawback is that there is a reduction in the durability of the PVD-treated components over a long time of usage [7]. In case of the hardfacing technique, the worn-out surfaces can be reconstructed, and further, the necessity for changing the parts is greatly reduced. However, the distortion effect produced by the plasma reduces the usage of this technique [8]. Another technique called thermal spray coating can be implemented for a vast range of substrates with reduced impact on the environment. But, only thin coatings can be achieved and in special cases (curved surfaces), this technique has a very low spray efficiency [9]. Laser cladding is one of the widely used surface treatment techniques which can produce a finite layer on the substrate material. This technique requires low energy and the laser cladded material has a better surface finish, consistent morphological behavior, low distortion effect, and high precision when compared with the other techniques [10–13]. Due to these advantages, this technique is employed in enhancing the service life of the components that operate in harsh environments.

Since corrosion resistance of SS410 steel is greatly affected by hostile environments, the cladding material should sustain this environment. Colmonoy alloys are nickel-based superalloys that have good resistance to corrosion. They offer better wear resistance, high hardness, greater impact strength, and high-temperature corrosion resistance [14]. Zhang et al. [15] analyzed the wear resistance of the laser cladded Colmonoy powder on the stainless steel 316 substrate. They reported that the laser cladded specimens showed a higher rate of wear resistance compared with the normal specimen. Jeyaprakash et al. [16] reported that the laser cladded Colmonoy depositions exhibit the hard laves phase. This phase contributes more towards facilitating the

hardness and wear resistance. Singh et al. [17] analyzed the tribo performance of Stellite, Colmonoy powders using High-Velocity Oxygen Fuel (HVOF) method and reported that the microhardness of the substrate is greatly enhanced by Colmonoy particles and also exhibits low erosion wear than the Stellite. The laser cladded Colmonoy particles have increased the wear resistance up to 49 times than the substrate [18]. F. Oliveria et al. [19] reported that the fatigue strength of the 4340-steel substrate is significantly improved by incorporating Colmonoy powders. Gnanasekaran et al. [20] investigated the tribological properties of Colmonoy-5 particles using hardfacing technique and concluded that the Colmonoy-5 coatings exhibited a greater resistance to wear, compared with the 316-LN substrate.

The major outcomes of the above literature are summarized as follows. They have used different surface treatment techniques like HVOF thermal spray, hardfacing, laser cladding for coating Colmonoy particles on different substrates. Further, it is evident that the laser cladding can produce a fine layer of deposition and Colmonoy coatings effects in improving the hardness, wear resistance, fatigue strength, and tribological behaviors of the substrate. However, the corrosion resistance of the Colmonoy-5 claddings at various time intervals considering the corroded morphology and surface roughness has not been addressed yet. This work is aimed to evaluate the corrosion resistance of the laser cladded Colmonoy-5 particles on the SS410 substrate at 0, 8, 14, and 36 h intervals followed by examining the microstructure, corroded morphology, nano hardness, and surface roughness of the cladded samples. The morphological structures of the cladded specimen were analyzed by using Field Emission Scanning Electron Microscope (FESEM) with respect to the elemental mapping obtained from the Energy-dispersive X-ray spectroscopy (EDS). Nanoindentation studies and Vickers hardness tests were carried out to evaluate the hardness at the base, cladded, and interface region. In addition, the surface roughness was measured and in an electrochemical environment, the corrosion test was carried out for different time durations and the results were compared with the SS410 substrate.

2 Experimentation

2.1 Materials

Martensitic stainless steel with grade 410 was selected as the substrate material for the laser cladding process. The as-received Colmonoy-5 alloy powder from the market was used as the cladding material. The morphology, shape, and size distribution of the Colmonoy-5 particles were examined using the FESEM technique as presented in Fig. 1. These particles have an average size of $125 \pm 15 \mu\text{m}$. The chemi-

Fig. 1 FESEM image of the as-received Colmonoy-5 powder particles

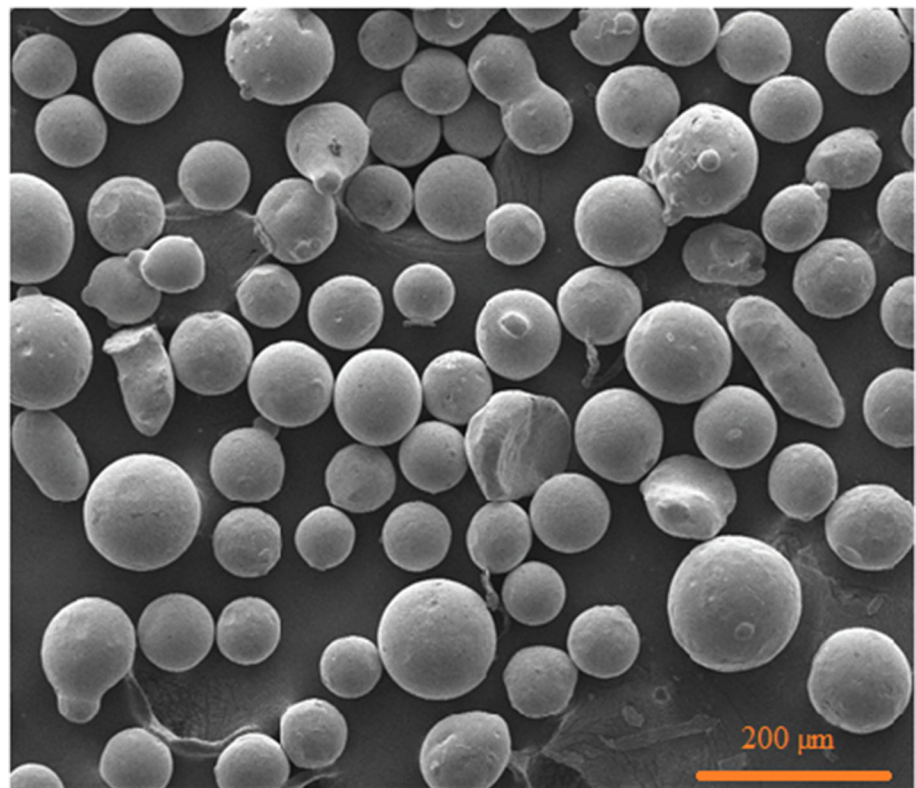


Table 1 Elemental composition of SS410 and Colmonoy-5 materials

Material	Ni (%)	P (%)	Cr (%)	Fe (%)	S (%)	B (%)	Si (%)	C (%)	Mn (%)
Substrate-SS410	0.75	0.04	13.5	BAL	0.03	–	1	0.15	1
Colmonoy-5	BAL	–	10.5	3.02	–	2.24	3.86	0.46	–

cal composition of the as-received Colmonoy-5 alloy powder and the SS410 substrate are tabulated in Table 1.

2.2 Chemicals

Before the cladding process, acetone was used to clean the substrate's surface for removing the surface impurities. After rinsing with the acetone, the samples were sandblasted with Al_2O_3 particles to obtain the surface roughness of 5 μm . This surface roughness ensures the good metallurgical bonding between the SS410 and Colmonoy-5 particles. After the cladding process, the cladded samples were polished by silicon carbide (SiC) sheets and diamond followed by electrolytic chemical etching using the 2 wt% of chromic acid (H_2CrO_4) solution for revealing the microstructure. The corrosion analysis was performed by preferring the test solution made by dissolving 3.5 wt% of sodium chloride in 100 ml of deionized water. The main reason for selecting NaCl for preparing the test solution is that the Cl^- ions are more belligerent and able to destroy the passivation film formed on the

metals by producing a notable and localized type of corrosion attack on it [21].

2.3 Laser Cladding Process

Ytterbium-doped Yttrium Aluminum Garnet (Yb: YAG) laser with a power output of 6 kW and a wavelength of 1060 nm has been used to perform the laser cladding. By using this laser, the as-received Colmonoy-5 powder particles were deposited on the sandblasted surface of the SS410 substrate. The schematic representation of the laser cladding technique is shown in Fig. 2. The cladding process parameters will have a great influence on the distribution of the Colmonoy-5 particles and deposition rate [22, 23]. After optimizing the process parameters, the cladding material was evenly deposited, producing a finite layer of deposition on the substrate material. The laser cladding process parameters are tabulated in Table 2. The cladded samples were collected after the cladding process and then cut into the cubic cross-section of 10 mm \times 10 mm. With the aid of JEOL 6500F FESEM, the microstructure of the cladded samples was ana-

Fig. 2 Schematic representation of the laser cladding process

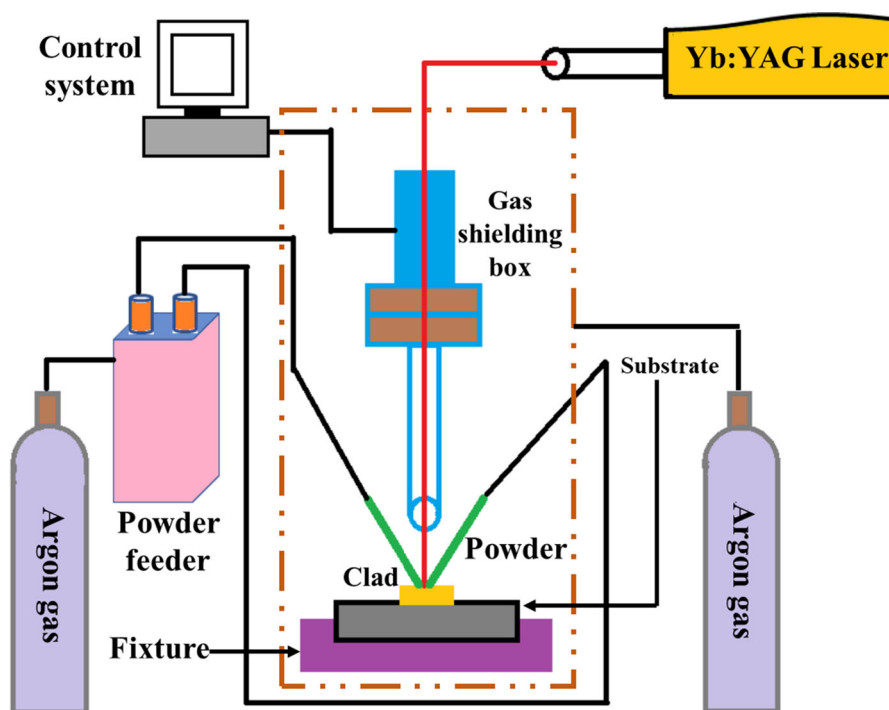


Table 2 Laser parameters used for cladding process

Material	Power	Feed rate	Scanning speed	Preheat temperature	Shielding gas flow	Carrier gas flow
Substrate-SS410	1400 W	9 g/min	600 mm/min	150 °C	25 L/min	6 SD @ 100,000/Pa

lyzed and by using the NOVA software, the curves of the Nyquist and bode plots were fitted.

2.4 Corrosion Analysis

The corrosion test was carried out in the electrolytic cell consisting of three electrodes connected to the workstation. Silver chloride (AgCl) electrode, platinum electrode, and the cladded samples were preferred as the reference, counter, and working electrode respectively. The working electrode was tightly kept against the Teflon disc to evaluate the resistance. With an exposing area of 100 mm², the surface of the cladded sample was unmasked in the electrolyte. Except the exposing surface, all other areas of the sample were sealed to avoid solution leakage.

The corrosion test procedure is as follows: Initially, the prepared electrolytic solution was poured into the electrolytic cell and the working electrode was kept at one end. After stabilizing the equilibrium potential, the scan rate was varied in the range between 0.05 to 1.2 V and the corresponding cyclic voltammetry curves were plotted. Finally, by using the Tafel method, the current density, and the corrosion potential were calculated at different time intervals (0, 8, 14, and 36 h). The EIS analysis was performed with the frequency range of 10⁶

to 10⁻² Hz. The microstructure of the substrate and cladded samples (various timings) were analyzed using FESEM with EDS. The hardness of the samples was examined by the Hysitron TI 980 Nanoindenter and Wolpert Wilson Instrument (402 MVD). The surface roughness after the corrosion process was evaluated using the white light interferometer and the captured images from this interferometer were processed using the Gwyddion software.

3 Results and Discussion

3.1 Structural Analysis

After laser cladding, the samples were collected and it is found that the Colmonoy-5 particles were distributed uniformly with a layer thickness of 600 μm. Figure 3a shows the optical microscopic image of the cross-sectional cladded samples representing the base, interface, and cladded regions. In the cladded regions, the cladded particles are evenly deposited with no defects or pores. The image obtained from the optical microscope for the cladded region is presented in Fig. 3b. It is seen that the cladded region consists of dendritic and interdendritic structures. The dendritic structure

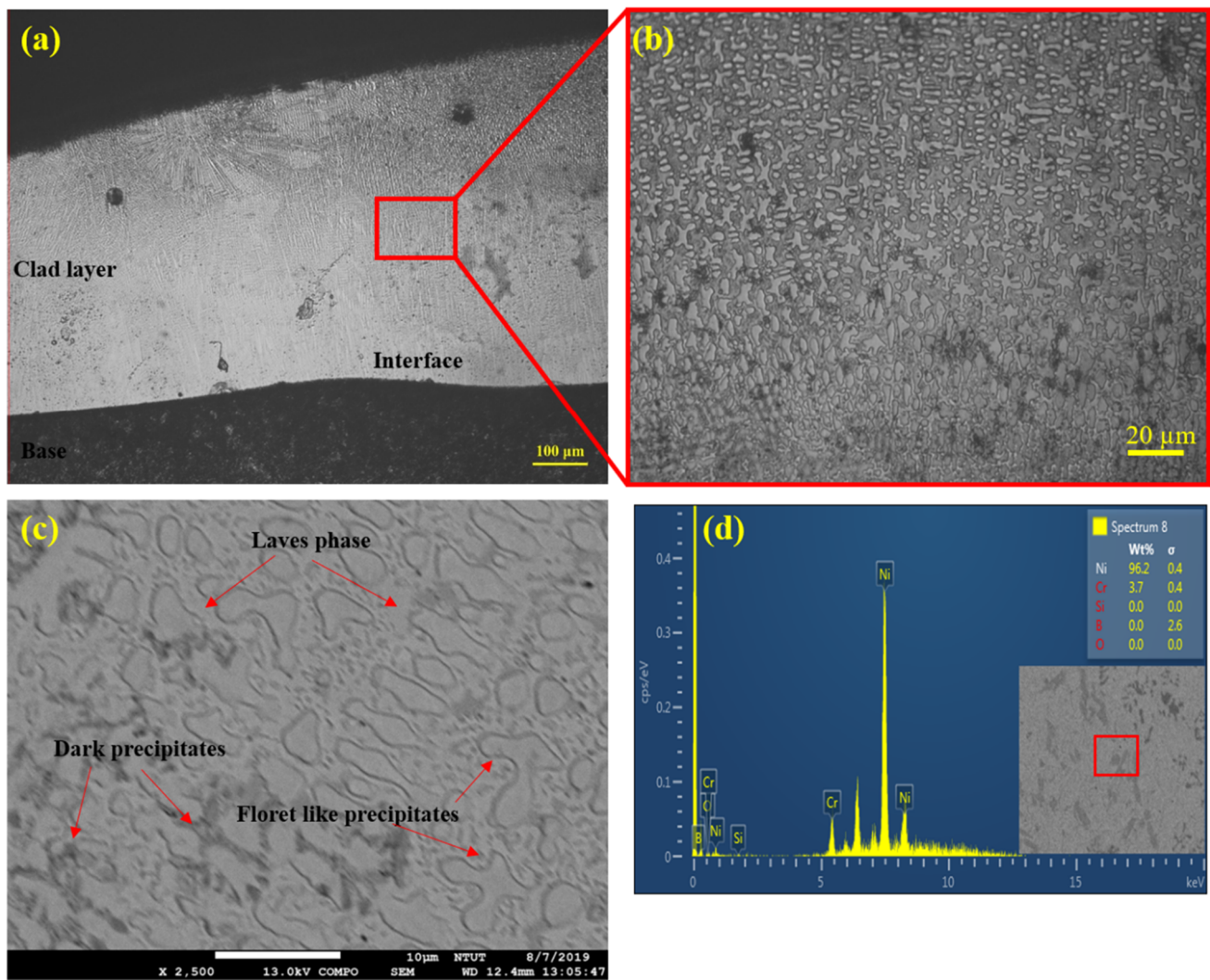


Fig. 3 **a** Optical microscopic image of the cross-sectioned sample representing the base, interface, and the clad region, **b** Optical image obtained at the clad region, **c** FESEM image representing the dark and floret like

precipitates formed at the clad region, **d** Elemental mapping obtained from EDS at the clad region (Inset: Image used for EDS scanning)

reveals the presence of the γ -nickel matrix, whereas the interdendritic structure represents the existence of precipitates of boride and carbide [24]. And also, the laser power (1400 W) causes the hardening of the dendritic structure besides the distribution of dark regions [25].

Figure 3c represents the FESEM image of the clad region. The laser clad Colmonoy-5 layer consists of the hard laves phase with dendritic and interdendritic structures in the γ -Ni matrix. The hard laves phases are said to be rich in $(\text{FeNi})_3\text{B}$ and nickel boride because the clad layer is Ni-based superalloy which contains nearly 75% of nickel. The dendritic and interdendritic structures are due to the dark and floret-like precipitates which represent the presence of carbides and borides of chromium [26]. These carbides and borides are distributed in the γ -nickel matrix of the clad

specimens. It is also found that the hard laves phases present in the clad regions with some intermetallic compounds like Ni_3Si and Ni_4B are responsible for enhancing the hardness and wear resistance of the specimen [27]. Thus, the obtained chromium-rich borides (floret-shaped structures) and chromium-rich carbides (dark or blocky structures) match with the outcomes of the microstructural analysis of Colmonoy-5 particles by Savanth et al. [28] and Gurumoorthy et al. [29]. In the floret-like structure, the chromium boride may present in three forms namely CrB , Cr_2B , and Cr_5B_3 respectively [30]. The same author (Jeyaprakash et al. [27]) have examined the phases of laser clad Colmonoy-5 particles on SS410 steel substrate using the XRD analysis. They have reported that the clad layer contains the Cr-rich carbides and boride precipitates in γ -Ni matrix with some

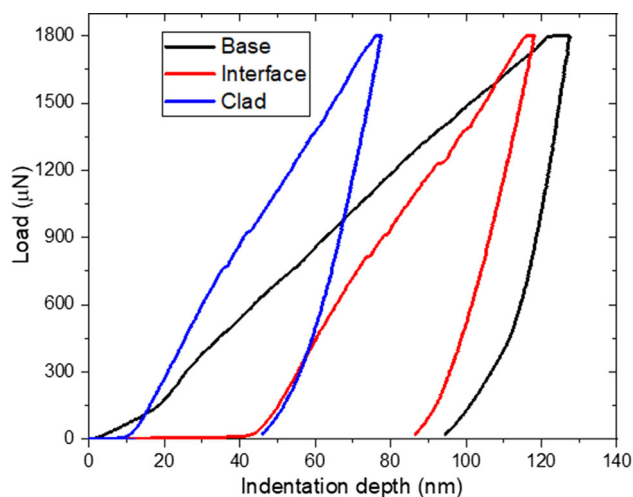


Fig. 4 Load to depth plot at the base, interface, and the clad region obtained from the nano hardness test

intermetallic compounds that aid in improving the hardness. Also, they revealed that formation of laves phase consisting of $(\text{FeNi})_3\text{B}$ and nickel boride since the deposited Colmonoy-5 is a nickel-based superalloy. The corresponding elemental mapping is done with the help of EDS as in Fig. 3d. It shows a high peak for Ni. This is due to the presence of γ -nickel matrix in the clad region and also in Colmonoy-5, the major component is nickel (~75%). The second highest peak is obtained for chromium since it contributes around 11.5% to Colmonoy-5. It also confirms the presence of chromium-rich carbides and floret-shaped chromium borides with interdendritic structure [24]. This boride helps in preventing crack formation in the clad region [31]. Other intermetallic compounds like Ni_3Si and Fe concentration help in improving the mechanical strength of the clad specimen.

3.2 Hardness Measurements

Hardness is an inherent property of a material that prevents deformation. It is a measure of resistance against plastic deformation and plays a vital role in determining wear resistance. The laser cladding technique is used to enhance the surface where the clad surface requires a hardness evaluation to evaluate its resistance [32]. The load to depth curves (Fig. 4) for the clad samples at the three regions were obtained using the nanoindentation analysis. These curves clearly depict the process of loading and unloading during deformation. The elastic and plastic deformations are obtained as a result of a gradual increase in the load from 0 to 1800 μN . During the unloading process, the elastic phase is recovered but the plastic deformation is maintained. Thus, the formation of indentation takes place in the sample [33].

From Fig. 4, the base region (SS410) experiences a higher indentation depth (~95 nm) compared to the interface and the

clad region. In the clad region, the indentation depth is nearly half the value of the base region. Generally, in this type of analysis, higher the depth, lower is the hardness [34]. For the three regions, the nano hardness value has been calculated. The clad region exhibits a high hardness value (5.48 GPa) compared with the interface (2.89 GPa) and the base (2.39 GPa) region. The hardness at the clad region is due to the formation of chromium-rich carbides and borides. The existence of floret-shaped precipitates containing Cr-rich borides in the clad region is responsible for improving the hardness, thereby enhancing the wear resistance of the samples [35]. Moreover, Balaguru et al. [36] and Gnanasekaran et al. [37] analyzed the hardness and wear resistance of the Colmonoy-5 coatings and concluded that the floret and dark precipitates of Cr-rich borides and carbides are responsible for enhancing the hardness property thereby improving the wear resistance offered and also same as our observations.

To further confirm that the Colmonoy-5 cladding layer provides better hardness than the SS410, the Vickers microhardness test was performed on the base, interface, and the clad layers using the Wolpert Wilson instrument. Figure 5 represents the formed micro indentations on the sample. The formed micro indentation profile from the top of the clad layer to the base material and the optical microscopic image of the sample's cross-section is shown in Fig. 5a and b, respectively. These indentations were obtained by applying the load of 0.5 kgf for the dwell time of 15 s. The microhardness profile and the corresponding indentation formed at the base, interface, and the clad layer is represented in Fig. 5c. From this figure, it can be seen that for the applied load, the indentation produced in the base region tends to be larger. There is a decreasing trend in the formed indentation at the interface, and clad layer (inset Fig. 5c). The clad region experiences a smaller indentation profile because it exhibits better hardness compared to the base and interface layers [38]. In addition, the average hardness values have been calculated and the values at the base, interface and the clad region are 208.57, 493.6, and 720.88 HV respectively. The Colmonoy-5 layer experiences a higher hardness value and it is nearly 3.5 times that of the value at the SS410 region. This is because of the chromium-rich carbide and boride precipitates that precipitated during the laser cladding of Colmonoy-5 particles [27, 39]. Thus, both the nanoindentation and the microhardness profiles revealed that the clad region exhibits better hardness compared with the SS410 substrate.

3.3 Corrosion Test

The corrosion test was carried out at ambient conditions on both base (SS410) and clad sample with the electrolytic solution made by dissolving 3.5 wt% NaCl in 100 ml of deionized water. This test was attempted to evaluate the corrosion resistance of clad samples at various periods such

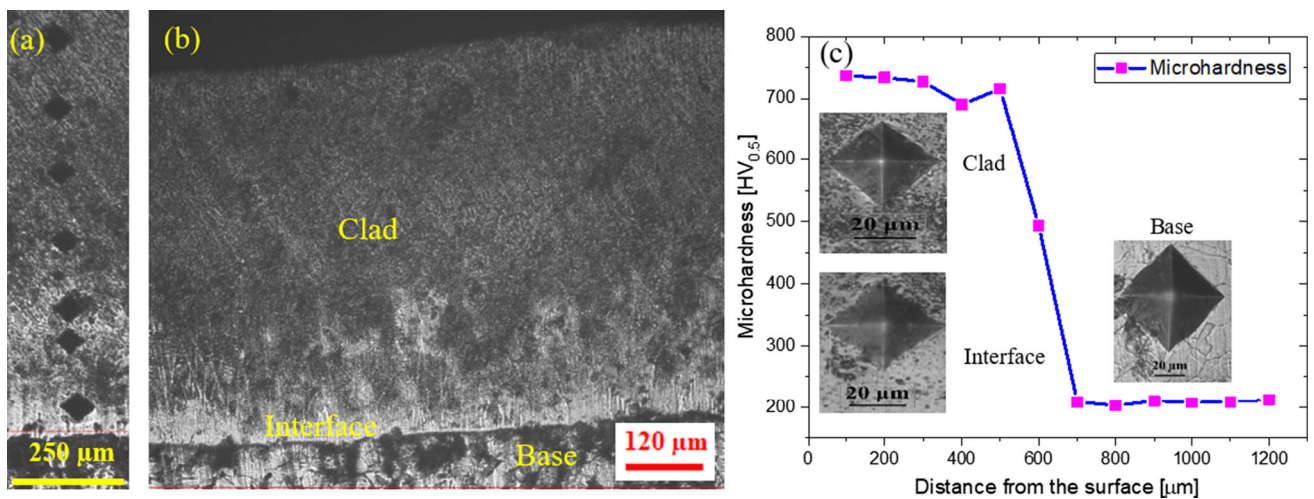
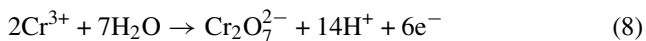
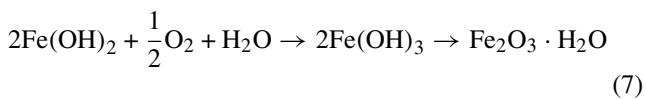
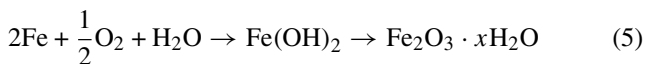
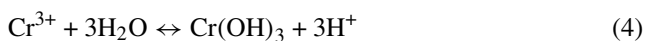
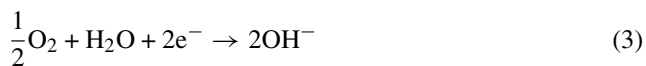
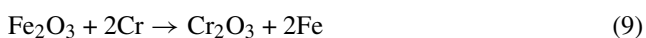


Fig. 5 **a** Microindentation from top of the clad to base material, **b** cross-sectioned optical microscopy picture showing with three different zones, **c** microhardness profile with three different indentation marks

as 0, 8, 14, and 36 h, respectively. Since SS410 is used in hostile environments, the mechanism of oxide formation is represented by Eqs. (1)–(8).



The formed oxide layer contains an outer layer made up of iron oxide followed by the inner layer of chromium oxide [40]. The net balance equations of the outer iron oxide formation are represented in Eqs. (5) and (7). The Eqs. (9)–(11) shows the net balance equations of the inner chromium oxide layer respectively.



The formed chromium oxide generally resists corrosion under normal conditions. But in the case of harsh environments, the formed oxide film loses its property to resist corrosion because this film reacts with CO₂, Cl⁻, H₂SO₄, H₂S, etc. produced in such environments and tends to form other compounds, thereby degrading the corrosion resistance property. The sulfides and chlorides present in the oil refinery plants readily react with the H⁺ ions produced during the oxide formation. These H⁺ ions react with the chlorides and sulfides to form corrosive acids such as HCl, H₂SO₄. At high temperatures, these acids react with the formed oxide film and as time passes, it minimizes the resistance offered by the film [41, 42]. If the working environment contains Cl⁻ ions (hydro turbines), its aggressive nature destroys the metal oxide film due to the significant localized corrosion attack [43].

Figure 6a and b represent the Tafel plots obtained as the result of the corrosion test carried out on both base and clad samples. The stability and resistance to corrosion are measured from this plot. Table 3 shows the parameters calibrated from the polarization curve for both samples. The Tafel plot obtained for the base and the clad samples for 0 h (raw samples) is shown in Fig. 6a. From this figure, the base sample experiences a higher current density (3.193 × 10⁻⁵ A/cm²) compared with the clad sample (4.447 × 10⁻⁶ A/cm²). This reduced current density shows that the cladding process results in a significant change in the resistance offered by the sample. On comparing the Tafel plots for different time intervals, the 8 h sample exhibits the minimum value of current density (2.463 × 10⁻⁷ A/cm²) than the 0, 14, 36 h samples. This reveals that the 8 h sample offers the maximum resistance to corrosion due to its very low current density and in general, all the clad samples (0, 8, 14, and 36 h) show notable resistance to corrosion than the

Table 3 Corrosion test data

Duration	<i>E</i> -current (V)	<i>I</i> -current (A/cm ²)
Base 0 h	− 0.471894454	$3.19279679 \times 10^{-5}$
Clad 0 h	− 0.420302773	4.447234×10^{-6}
Clad 8 h	− 0.153926146	$2.46307193 \times 10^{-7}$
Clad 14 h	− 0.179180815	$5.65421974 \times 10^{-7}$
Clad 36 h	− 0.243166384	$2.22222967 \times 10^{-6}$

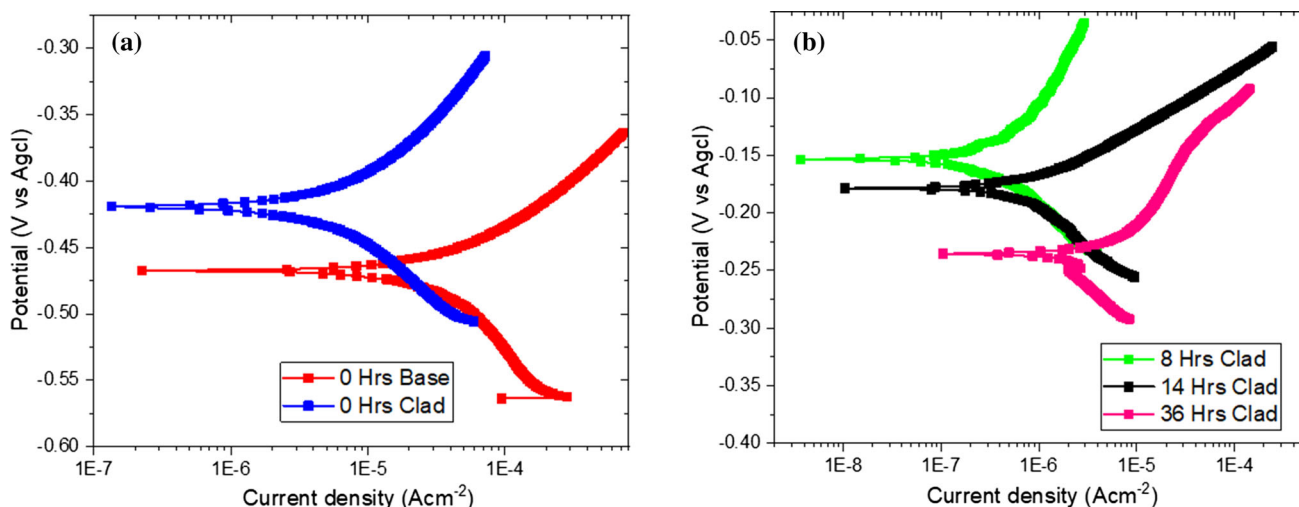
SS410 substrate. This is because of the presence of electrochemically stable chromium-rich carbides and borides in the clad sample. Further, Moghaddasi et al. [44] and Mele et al. [45] also confirmed that these electrochemically stable compounds aid in the formation of strong and stable passive that enhances the corrosion resistance property of the Colmonoy coatings in harsh environments.

Figure 7a and b show the corroded surface and the elemental mapping obtained from FESEM and EDS for 0 h (raw samples) SS410 substrate. This sample is said to have higher oxide content (38.85%) with an irregular crystalline structure. The crystalline morphology on the corroded surface along with the elements present in the clad samples at various time intervals are shown in Fig. 8a–h. It is reported that the 8 h sample has an acceptable amount of Boron and thus it forms a finite structure exhibiting high resistance to corrosion than the other intervals. The 0, 14, and 36 h sample tends to have a higher amount of Boron. This increased amount than the acceptable limit results in the deformation of the formed finite structure and starts to become fragile followed by the formation of patches. As time goes on, these patches will start to leave the surface. Table 4 presents the

elemental composition of the SS410 and the clad samples after the corrosion test. The mechanism of passivation formed on the clad sample is shown in Fig. 9. Hence, the 8 h sample is seen to have higher resistance to corrosion due to its lower current density.

3.4 Electrochemical Impedance Spectroscopy (EIS) Analysis

The EIS analysis was performed to evaluate the charge transfer resistance for both the base and clad samples. The results of EIS analysis are represented by the Nyquist and Bode plots as in Fig. 10a–d. The Nyquist plots exhibit a single capacitive loop within the operating frequency range. It is evident that the electrode reaction is dominated by the electrochemical reaction [46]. In general, the greater semicircular area will have more impedance thereby exhibiting a higher resistance towards corrosion [47, 48]. Figure 10a shows the Nyquist plot for the base and clad specimen for zero hours (raw samples). It can be seen that the loop area of the base is very much smaller than that of the clad specimen. The clad sample shows greater resistance to corrosion than the base sample. The Nyquist plot for 8, 14, 36 h clad specimens is shown in Fig. 10c. The 8 h clad sample has the maximum arc radius compared with other samples. This is due to the presence of finite crystal structure and an acceptable amount of Boron which shows a maximum resistance towards corrosion. As the time increases (14 and 36 h) the formed film starts to break into small patches which may be the reason for the reduction in the charge transfer resistance. The bode plots obtained for both the samples are shown in Fig. 10b and d. The covered area of the curves in the bode

**Fig. 6** Tafel graph obtained for **a** 0 h base and clad specimens, **b** 8, 14, and 36 h clad specimens

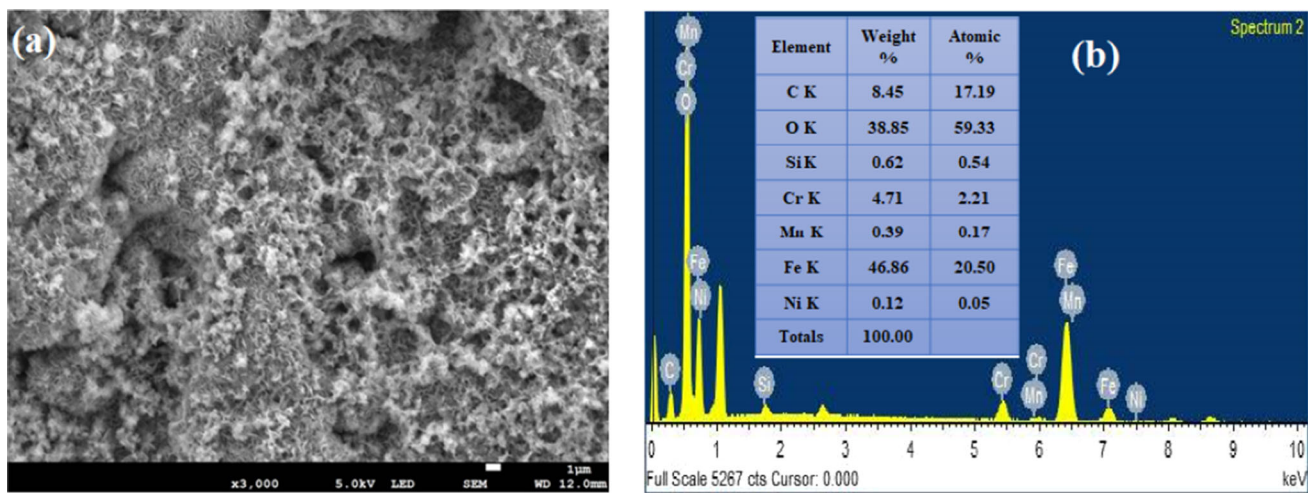


Fig. 7 a FESEM image of corroded surface, b Corresponding elemental mapping of 0 h base sample

Table 4 The elemental compositions at the surfaces of different specimens after corrosion test

	Element	C K	O K	Si K	Cr K	Mn K	Fe K	Ni K	B K	Totals
Base 0 h	Weight%	8.45	38.85	0.62	4.71	0.39	46.86	0.12	–	100.00
	Atomic%	17.19	59.33	0.54	2.21	0.17	20.50	0.05	–	
Clad 0 h	Weight%	13.74	1.98	2.17	14.84	–	10.28	37.72	19.26	100.00
	Atomic%	26.99	2.92	1.82	6.73	–	4.34	15.16	42.04	
Clad 8 h	Weight%	16.74	1.32	3.72	4.17	–	10.02	58.58	5.46	100.00
	Atomic%	41.35	2.45	3.93	2.38	–	5.32	29.60	14.98	
Clad 14 h	Weight%	4.83	1.40	1.39	37.03	–	12.02	32.88	10.45	100.00
	Atomic%	13.44	2.92	1.65	23.80	–	7.19	18.71	32.28	
Clad 36 h	Weight%	31.70	1.42	1.30	7.79	–	8.75	34.37	14.68	100.00
	Atomic%	52.53	1.77	0.92	2.98	–	3.12	11.65	27.03	

plots is directly proportional to the resistance to corrosion [49]. On comparing these figures, the clad samples have better resistance towards corrosion and among the different time intervals, the 8 h clad sample experiences a wider area covered by the curves. Thus, it shows the maximum corrosion resistance than other samples, due to the effect of the formation of floret-like Cr-rich precipitates.

The corresponding electric equivalent circuit is schematically represented in Fig. 10d. R_p and R_s represent the resistance due to polarization and solution, whereas the constant phase element is denoted as CPE. The elemental parameter values calculated from the equivalent circuit for both the samples are tabulated in Table 5. The value of R_p is directly proportional to the corrosion resistance. The higher the R_p value, the greater will be the resistance towards corrosion [50, 51]. From Table 5, it can be inferred that the clad samples tend to have higher R_p values compared to the base sample. In addition, 8 h sample results in maximum R_p value (32,312) than 0, 14 and 36 h sample. And also, Zeng et al. [52]

and Li et al. [53] proved that the Colmonoy coatings exhibit higher R_p values due to the formation of carbide and borides precipitates and their results are similar to our results because the clad Colmonoy coatings have maximum R_p values. Thus from the Nyquist and Bode plots, the clad sample experiences a significant improvement in resistance towards corrosion due to the effects of the laser clad Colmonoy-5 particles.

3.5 Surface Roughness Evaluation

Surface roughness is a major key factor that influences the corrosion resistance of the materials [54, 55]. This type of analysis is carried out by calculating the surface roughness value of both base and clad samples, which in turn decides the resistance towards corrosion. The 3D surface plot and the corresponding Scanning Probe Microscopy (SPM) images taken at the base and clad region after the cladding process are shown in Fig. 11a–d. From this, it

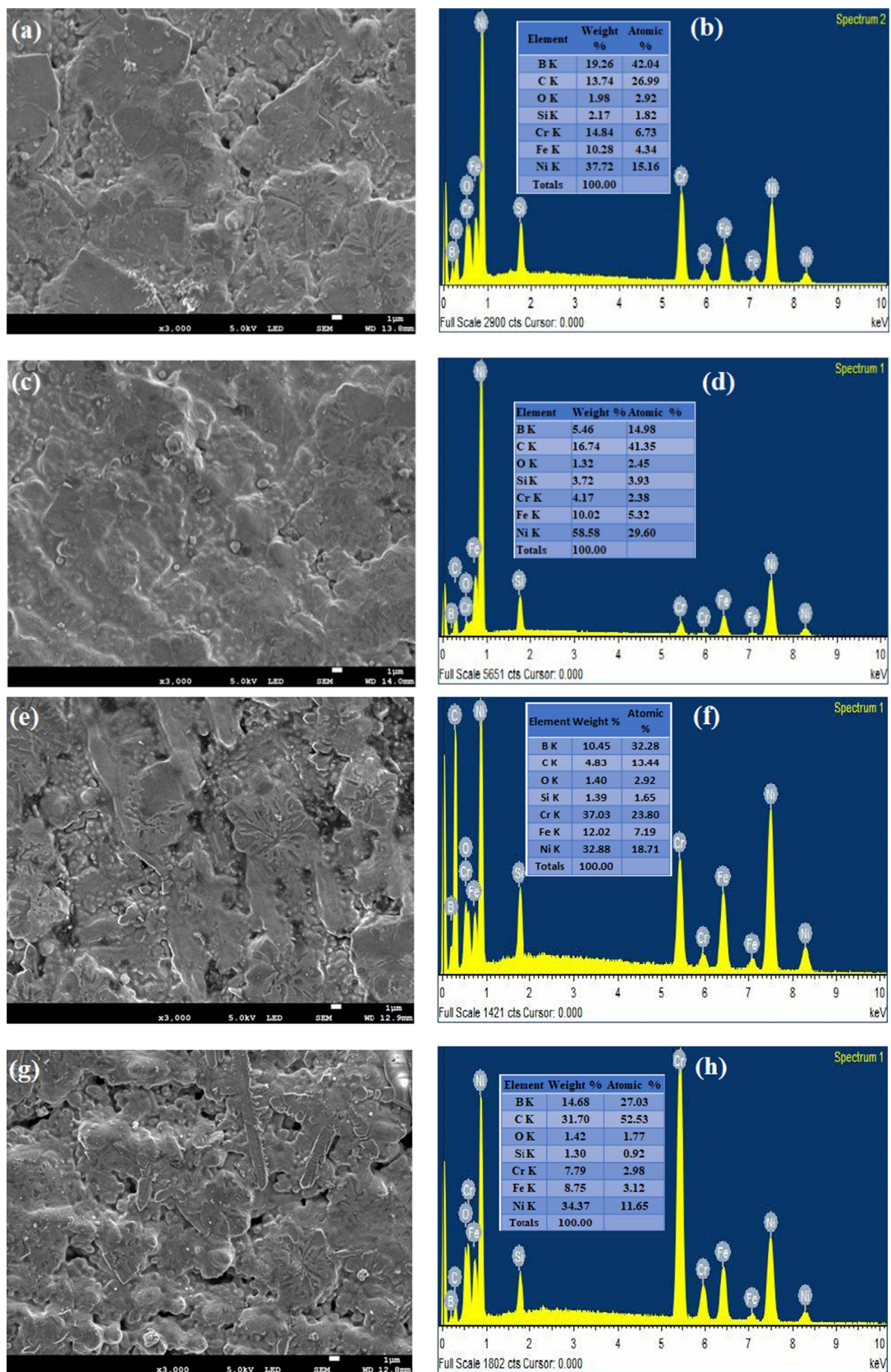


Fig. 8 FESEM image of corroded surface and the corresponding elemental mapping of cladded specimens at (a–b) 0 h, (c–d) 8 h, (e–f) 14 h and (g–h) 36 h respectively

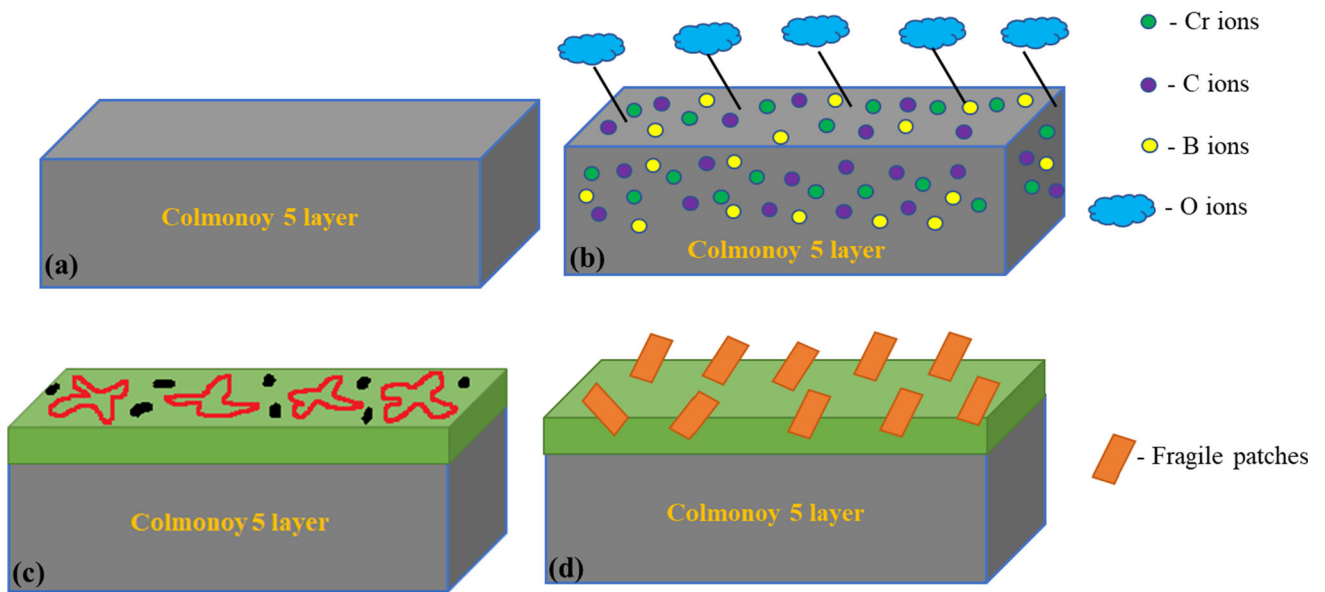


Fig. 9 Passivation film formation during the corrosion process, **a** Laser clad Colmonoy-5 layer, **b** Cr, C and B ions of the Colmonoy 5 reacts with the oxygen ions, **c** Passivation film formation on the Colmonoy 5 layer consisting of dark and floret like structures due to the Cr rich carbide and borides, **d** Fragile patches leaves the surface

Table 5 Parameter values of different elements used in EIS analysis

Duration	Element Parameter	Rs R	Rp R	CPE Y0	N
Base 0 h	Value	12.586	125.39	0.0034998	0.61719
($\chi^2 = 1.1475$)	Estimated error (%)	2.776	4.923	9.929	4.077
Clad 0 h	Value	10.51	1636.2	9.7027E-05	0.66577
($\chi^2 = 0.89456$)	Estimated error (%)	4.439	2.887	6.688	1.449
Clad 8 h	Value	12.048	32.312	2.498E-05	0.75302
($\chi^2 = 0.30457$)	Estimated error (%)	2.507	2.520	2.298	0.476
Clad 14 h	Value	9.3984	3429.3	6.2378E-05	0.69639
($\chi^2 = 0.5687$)	Estimated error (%)	3.626	2.360	4.492	0.933
Clad 36 h	Value	8.7586	1731.3	0.0001054	0.6262
($\chi^2 = 1.8602$)	Estimated error (%)	8.384	4.853	9.870	2.174

can be seen that the calculated roughness value at the base region (19.4 nm) is very much higher than the roughness value at the clad region (4.69 nm). The clad region value is nearly one-fourth the value at the base region. This reduced roughness value indicates that the Colmonoy-5 particles are evenly distributed during the cladding process. It also defines that the formed passivation film has a finite structure which results in a better surface finish in the clad sample [56].

For the corroded sample, the 3D surface plot and its 2D graph obtained using the white light interferometer for both

the base and different time interval clad samples are shown in Fig. 12a–j. The calculated roughness values for the base and clad samples at various timings are tabulated in Table 6. On comparing the roughness values of the 0 h base (raw sample) and the clad sample, the clad sample exhibits a reduced roughness value ($0.5136 \pm 0.0535 \mu\text{m}$) than the base ($0.8186 \pm 0.0793 \mu\text{m}$). It proves that the cladding process results in a significant reduction in the surface roughness, thereby enhancing the corrosion resistance property [57, 58]. On the other hand, the 8 h clad samples show a minimum roughness value ($0.3161 \pm 0.0494 \mu\text{m}$)

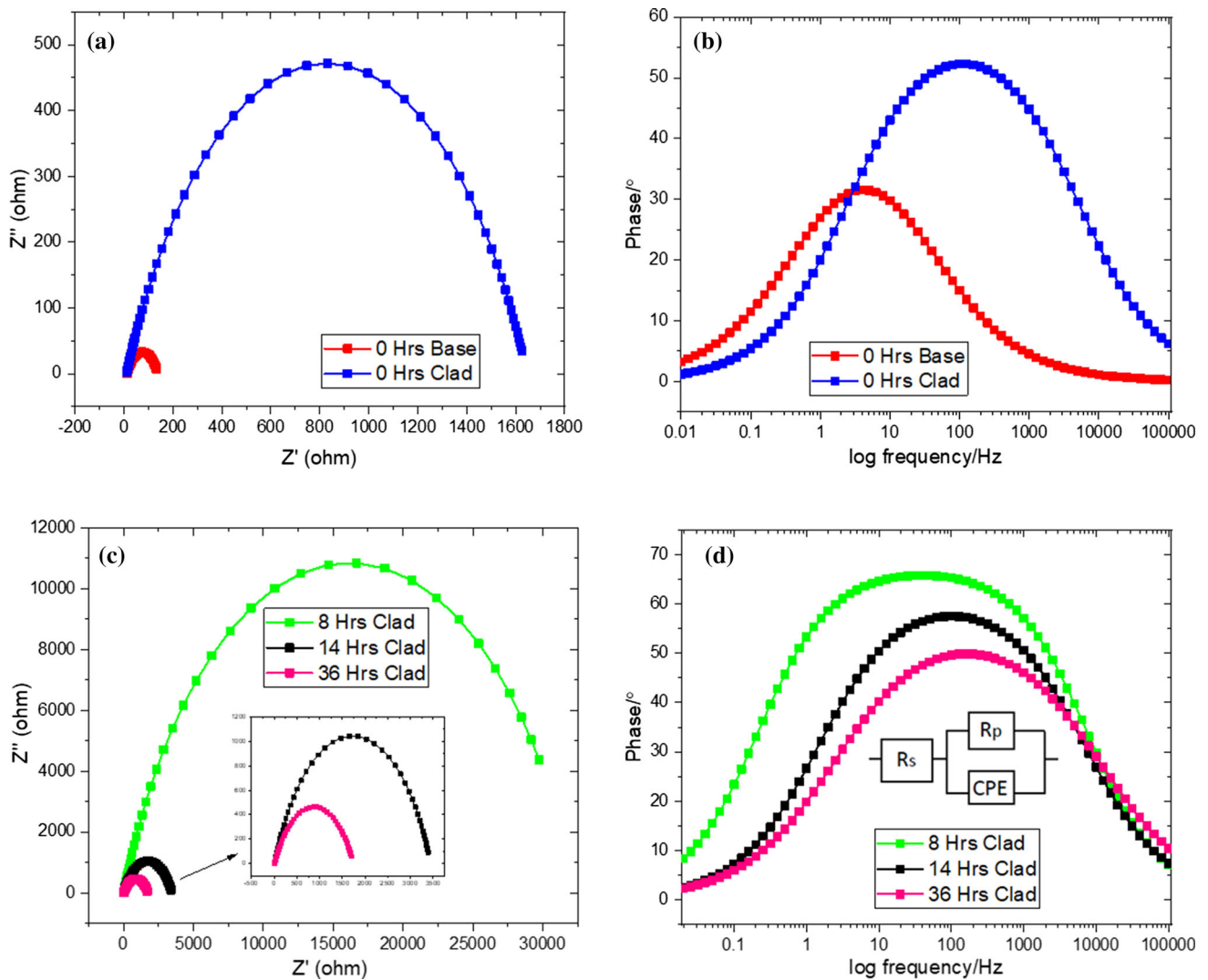


Fig. 10 Nyquist and Bode plots obtained from the EIS for both base and the various timing treated cladded samples

than 14 and 36 h samples due to the formation of a better surface consisting of chromium-rich borides. Further, the cladded samples experience better surfaces with lower surface roughness value and match with Jeyaprakash et al. [10]. For higher time intervals, the formed film becomes brittle and starts to run away from the surface as patches, followed by damaging the finite crystal structure. Hence the cladding process improves the corrosion resistance of the samples.

Table 6 Roughness values of base and cladded surface after corrosion test

Specimens	Roughness value— R_a (μm)
Base—0 h	0.8186 ± 0.0793
Clad—0 h	0.5136 ± 0.0535
Clad—8 h	0.3161 ± 0.0494
Clad—14 h	0.3998 ± 0.1229
Clad—36 h	0.4636 ± 0.1918

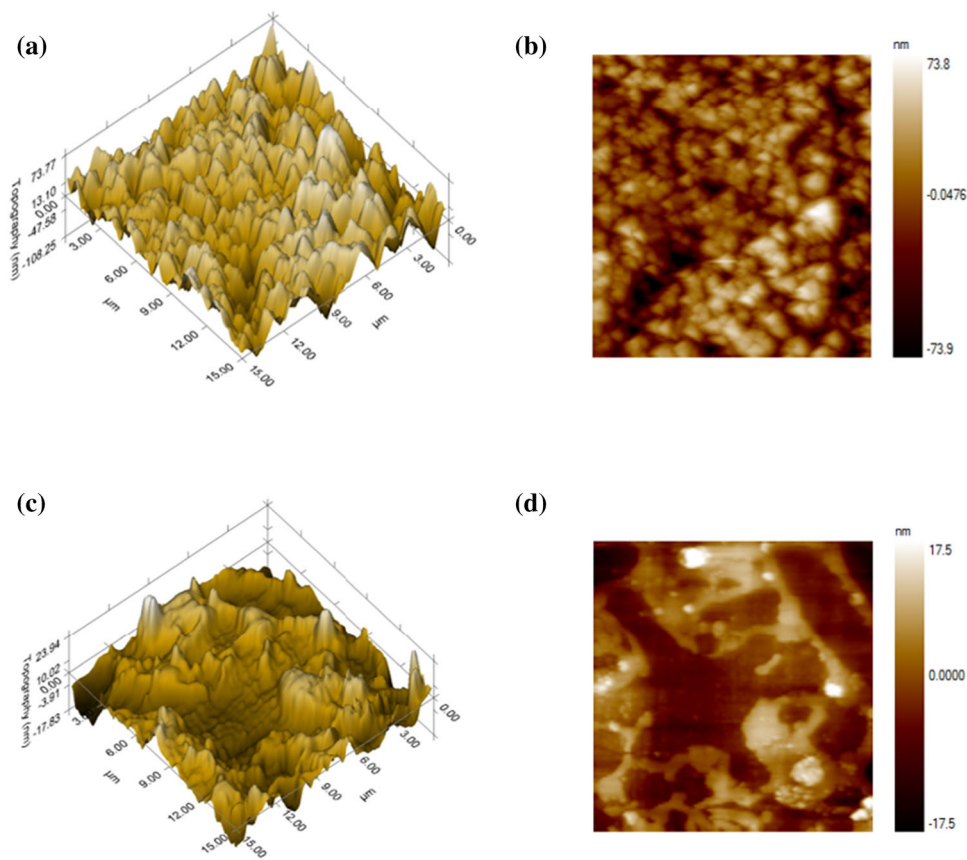


Fig. 11 3D surface plot and the corresponding SPM images obtained at the base (**a** and **b**), the clad (**c** and **d**) before corrosion test

4 Conclusions

The laser cladding process was carried out by depositing Colmonoy-5 particles on the SS410 substrate. The resulting microstructures in the cladded samples were analyzed by the FESEM technique followed by the corresponding elemental mapping with the EDS. The nanoindentation, the microhardness, and the surface roughness analysis were performed on the corroded sample to evaluate its hardness and roughness values at the three regions. In an electrochemical environment, the corrosion tests and EIS analysis were done for the cladded samples to reveal their corrosion resistance. The major conclusions of this work are as follows:

- The structural analysis reports that a uniform coating of Colmonoy-5 particles was deposited on the SS410 substrate. The cladding layer exhibited dark and floret-like structures due to the presence of Cr-rich precipitates of carbides and borides which was further confirmed by the EDS analysis.
- From the nanoindentation study, the hardness of the samples has been evaluated. On comparing the base and

cladded samples, the cladded samples are found to experience a higher hardness than the base due to the existence of chromium boride and carbide in the cladded region and thus resulting in better wear resistance. The Vickers micro indentation study also confirms that the clad region exhibits a maximum value of hardness (720.88 HV) than the base and interface regions.

- The result of corrosion analysis reveals that the 8 h cladded sample has the maximum corrosion resistance due to the formation of stable passivation film without deforming the finite crystalline structure of the cladded samples.
- The Nyquist and Bode plots of EIS analysis consist of a single loop where the cladded samples experience a major resistance to corrosion due to the large arc radius. In addition, the equivalent circuit results in a high polarization resistance for the 8 h sample which in turn confirms that this sample provides a better resistance towards corrosion.
- From the surface roughness analysis, it is evident that the low roughness value is obtained for the cladded samples compared with the base. And also, 8 h sample provides the maximum resistance to corrosion due to the formation of a fine surface consisting of Cr-borides.

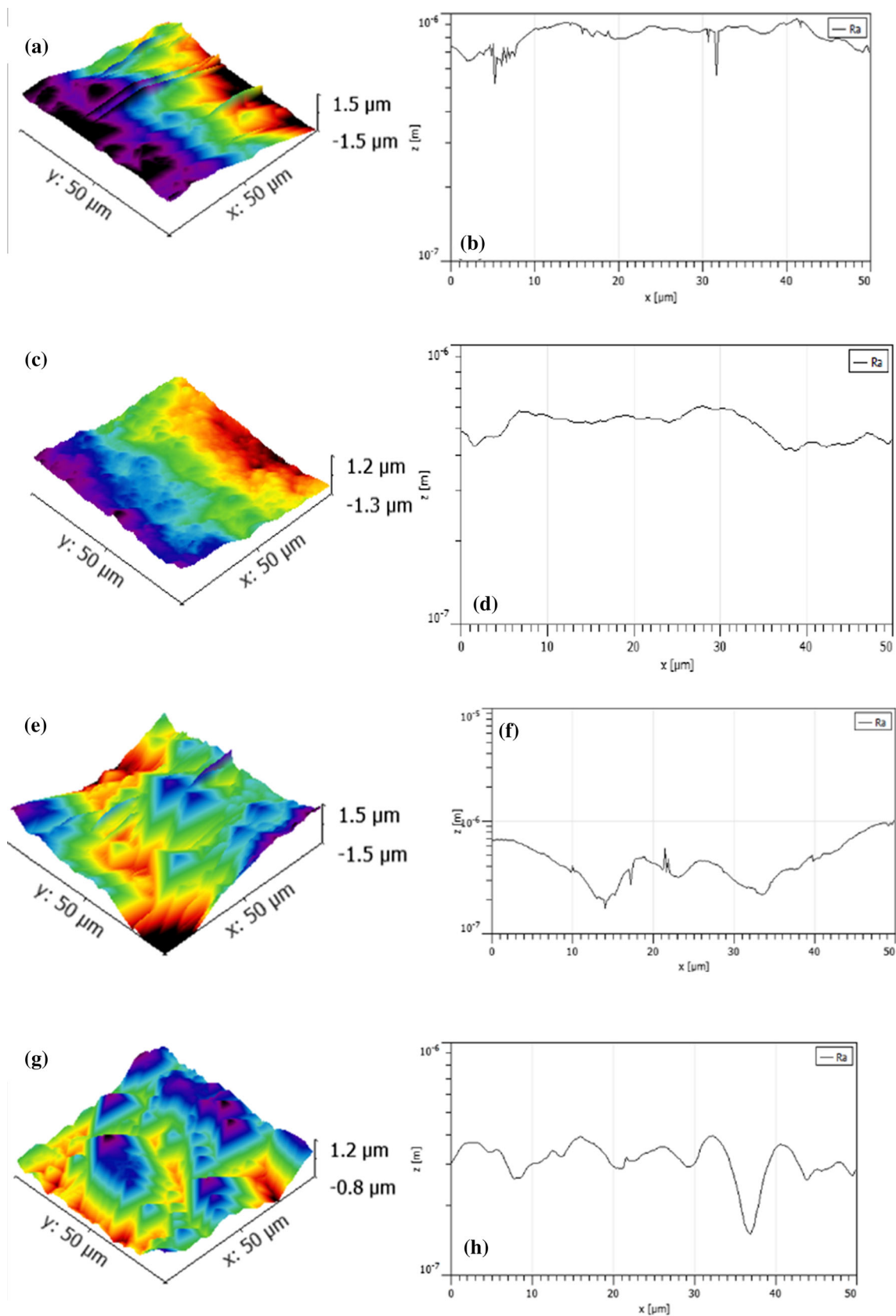


Fig. 12 Roughness of corroded 3D surface and its corresponding 2D plot obtained from white light interferometer for (a, b) base 0 h, clad (c, d) 0 h, (e, f) 8 h, (g, h) 14 h and (i, j) 36 h treated clad specimens

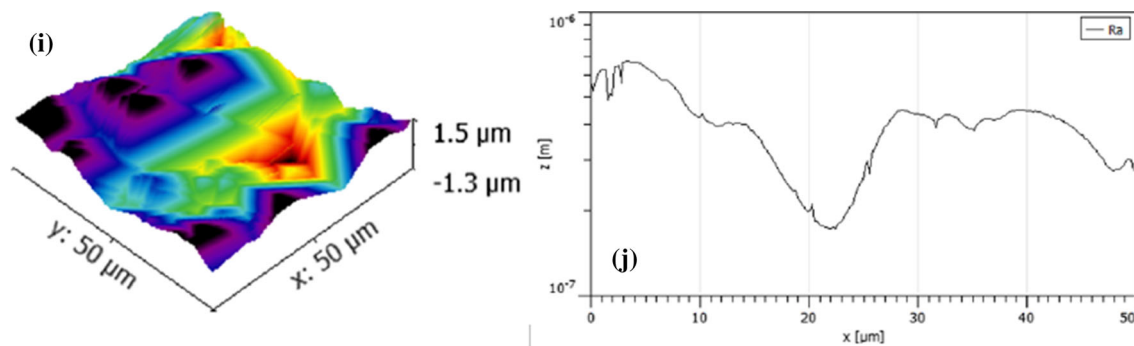


Fig. 12 continued

Thus, laser cladding of Colmonoy-5 particles improves the hardness, corrosion resistance and can be implemented in severe aggressive environments for increasing the working life and durability of components.

Acknowledgments We are grateful for the support from the Ministry of Science and Technology, Taiwan and Additive Manufacturing Center for Mass Customization Production, National Taipei University of Technology, Taiwan for providing the financial support.

Data Availability The experimental datasets obtained from this research work and then the analysed results during the current study are available from the corresponding author on reasonable request.

Declaration

Conflict of interest The authors declare that they have no known competing financial interests or personal relationships.

References

- Momeni, A.; Dehghani, K.; Heidari, M.; Vaseghi, M.: Modeling the flow curve of AISI 410 martensitic stainless steel. *J. Mater. Eng. Perform.* **21**(11), 2238–2243 (2012)
- Bansal, A.; Singh, J.; Singh, H.; Goyal, D.K.: Influence of thickness of hydrophobic polytetrafluoroethylene (PTFE) coatings on cavitation erosion of hydro-machinery steel SS410. *Wear* **29**, 203886 (2021)
- Taji, I.; Moayed, M.H.; Mirjalili, M.: Correlation between sensitization and pitting corrosion of AISI 403 martensitic stainless steel. *Corros. Sci.* **1**(92), 301–308 (2015)
- Lu, S.Y.; Yao, K.F.; Chen, Y.B.; Wang, M.H.; Ge, X.Y.: Influence of heat treatment on the microstructure and corrosion resistance of 13 wt pct Cr-type martensitic stainless steel. *Metall. Mater. Trans. A* **46**(12), 6090–6102 (2015)
- Lu, S.Y.; Yao, K.F.; Chen, Y.B.; Wang, M.H.; Shao, Y.; Ge, X.Y.: Effects of austenitizing temperature on the microstructure and electrochemical behavior of a martensitic stainless steel. *J. Appl. Electrochem.* **45**(4), 375–383 (2015)
- Tumbull, A.; de Santa Maria, M.S.; Thomas, N.D.: The effect of H₂S concentration and pH on hydrogen permeation in AISI 410 stainless steel in 5% NaCl. *Corros. Sci.* **29**(1), 89–104 (1989)
- Mehran, Q.M.; Fazal, M.A.; Bushroa, A.R.; Rubaiee, S.: A critical review on physical vapor deposition coatings applied on different engine components. *Crit. Rev. Solid State Mater. Sci.* **43**(2), 158–175 (2018)
- Ahn, D.G.: Hardfacing technologies for improvement of wear characteristics of hot working tools: a review. *Int. J. Precis. Eng. Manuf.* **14**(7), 1271–1283 (2013)
- Hardwicke, C.U.; Lau, Y.C.: Advances in thermal spray coatings for gas turbines and energy generation: a review. *J. Therm. Spray Technol.* **22**(5), 564–576 (2013)
- Jeyaprakash, N.; Yang, C.H.; Tseng, S.P.: Characterization and tribological evaluation of NiCrMoNb and NiCrBSiC laser cladding on near- α titanium alloy. *Int. J. Adv. Manuf. Technol.* **106**(5), 2347–2361 (2020)
- Jeyaprakash, N.; Yang, C.H.: Comparative study of NiCr-FeMoNb/FeCrMoVC laser cladding process on nickel-based superalloy. *Mater. Manuf. Process.* **35**(12), 1383–1391 (2020)
- Davim, J.P. (ed.): *Laser in Manufacturing*. Wiley, New Jersey (2013)
- Santo L, Davim J.: *Laser cladding: an overview*. (2010)
- La Barbera-Sosa, J.G.; Santana, Y.Y.; Moreno, E.; Cuadrado, N.; Caro, J.; Renault, P.O.; Le Bourhis, E.; Staia, M.H.; Puchi-Cabrera, E.S.: Effect of spraying distance on the microstructure and mechanical properties of a Colmonoy 88 alloy deposited by HVOF thermal spraying. *Surf. Coat. Technol.* **205**(7), 1799–1806 (2010)
- Zhang, H.; Shi, Y.; Kutsuna, M.; Xu, G.J.: Laser cladding of Colmonoy 6 powder on AISI316L austenitic stainless steel. *Nucl. Eng. Des.* **240**(10), 2691–2696 (2010)
- Jeyaprakash, N.; Yang, C.H.; Ramkumar, K.R.: Microstructure and wear resistance of laser clad Inconel 625 and Colmonoy 6 depositions on Inconel 625 substrate. *Appl. Phys. A* **126**, 1–1 (2020)
- Singh, J.; Kumar, S.; Mohapatra, S.K.: Erosion tribo-performance of HVOF deposited Stellite-6 and Colmonoy-88 micron layers on SS-316L. *Tribol. Int.* **147**, 105262 (2020)
- Jeyaprakash, N.; Yang, C.H.; Tseng, S.P.: Wear tribo-performances of laser cladding colmonoy-6 and stellite-6 micron layers on stainless steel 304 using Yb: YAG disk laser. *Met. Mater. Int.* **13**, 1–4 (2019)
- Oliveira, F.; Hernandez, L.; Berros, J.A.; Villalobos, C.; Pertuz, A.; Cabrera, E.P.: Corrosion–fatigue properties of a 4340 steel coated with Colmonoy 88 alloy, applied by HVOF thermal spray. *Surf. Coat. Technol.* **140**(2), 128–135 (2001)
- Gnanasekaran, S.; Padmanaban, G.; Balasubramanian, V.: Effect of laser power on metallurgical, mechanical and tribological characteristics of hardfaced surfaces of nickel-based alloy. *Lasers Manuf. Mater. Process.* **4**(4), 178–192 (2017)
- Kumar, N.; Fusco, M.; Komarasamy, M.; Mishra, R.S.; Bourham, M.; Murty, K.L.: Understanding effect of 3.5 wt.% NaCl on the corrosion of Al_{0.1}CoCrFeNi high-entropy alloy. *J. Nucl. Mater.* **495**, 154–163 (2017)



22. Davim, J.P.; Oliveira, C.; Cardoso, A.: Predicting the geometric form of clad in laser cladding by powder using multiple regression analysis (MRA). *Mater. Des.* **29**(2), 554–557 (2008)
23. Onwubolu, G.C.; Davim, J.P.; Oliveira, C.; Cardoso, A.: Prediction of clad angle in laser cladding by powder using response surface methodology and scatter search. *Opt. Laser Technol.* **39**(6), 1130–1134 (2007)
24. Kesavan, D.; Kamaraj, M.: The microstructure and high temperature wear performance of a nickel base hardfaced coating. *Surf. Coat. Technol.* **204**(24), 4034–4043 (2010)
25. Hemmati, I.; Ocelik, V.; Csach, K.; De Hosson, J.T.: Microstructure and phase formation in a rapidly solidified laser-deposited Ni-Cr-B-Si-C hardfacing alloy. *Metall. Mater. Trans. A.* **45**(2), 878–892 (2014)
26. Hemmati, I.; Rao, J.C.; Ocelik, V.; De Hosson, J.T.: Electron microscopy characterization of Ni-Cr-B-Si-C laser deposited coatings. *Microsc. Microanal.* **19**(1), 120–131 (2013)
27. Jeyaprakash, N.; Yang, C.H.; Ramkumar, K.R.; Sui, G.Z.: Comparison of microstructure, mechanical and wear behaviour of laser clad stainless steel 410 substrate using stainless steel 420 and Colmonoy 5 particles. *J. Iron. Steel Res. Int.* **27**(12), 1446–1455 (2020)
28. Savanth, T.; Singh, J.; Gill, J.S.: Laser power and scanning speed influence on the microstructure, hardness, and slurry erosion performance of Colmonoy-5 claddings. *Proc. Inst. Mech. Eng. Part L J. Mater. Des. Appl.* **234**(7), 947–961 (2020)
29. Gurumoorthy, K.; Kamaraj, M.; Rao, K.P.; Rao, A.S.; Venugopal, S.: Microstructural aspects of plasma transferred arc surfaced Ni-based hardfacing alloy. *Mater. Sci. Eng. A* **456**(1–2), 11–19 (2007)
30. Hemmati, I.; Ocelik, V.; De Hosson, J.T.: Evolution of microstructure and properties in laser cladding of a Ni-Cr-B-Si hardfacing alloy. *Contact Mech. Surf. Treat. X.* **19**, 287–296 (2011)
31. Gnanasekaran, S.; Padmanaban, G.; Balasubramanian, V.; Kumar, H.; Albert, S.K.: Correlation between travel speed, microstructure, mechanical properties and wear characteristics of Ni-based hardfaced deposits over 316LN austenitic stainless steel. *High Temp. Mater. Process.* **2019**(38), 16–29 (2019)
32. Davim, J.P.; Oliveira, C.; Cardoso, A.: Laser cladding: an experimental study of geometric form and hardness of coating using statistical analysis. *Proc. Inst. Mech. Eng. Part B J. Eng. Manuf.* **220**(9), 1549–1554 (2006)
33. Tao, Y.F.; Jun, L.I.; Lü, Y.H.; Hu, L.F.: Residual stress distribution in different depths of TiNi/Ti₂Ni-based laser clad coating prepared at different environmental temperatures. *Trans. Nonferrous Met. Soc. China* **27**(9), 2043–2054 (2017)
34. Hu, H.X.; Guo, X.M.; Zheng, Y.G.: Comparison of the cavitation erosion and slurry erosion behavior of cobalt-based and nickel-based coatings. *Wear* **15**(428), 246–257 (2019)
35. da Silva, L.J.; Scheuer, C.J.; D'Oliveira, A.S.: Effect of microstructure on wear performance of NiCrSiBC coatings. *Wear* **15**(428), 387–394 (2019)
36. Balaguru, S.; Murali, V.; Chellapandi, P.; Gupta, M.: Effect of dilution on micro hardness of Ni–Cr–B–Si alloy hardfaced on austenitic stainless steel plate for sodium-cooled fast reactor applications. *Nucl. Eng. Technol.* **52**(3), 589–596 (2020)
37. Gnanasekaran, S.; Padmanaban, G.; Balasubramanian, V.; Kumar, H.; Albert, S.K.: Laser hardfacing of colmonoy-5 (Ni-Cr-Si-BC) powder onto 316LN austenitic stainless steel: effect of powder feed rate on microstructure, mechanical properties and tribological behavior. *Lasers Eng.* **1**, 42 (2019)
38. Desale, G.R.; Paul, C.P.; Gandhi, B.K.; Jain, S.C.: Erosion wear behavior of laser clad surfaces of low carbon austenitic steel. *Wear* **266**(9–10), 975–987 (2009)
39. Miguel, J.M.; Guilemany, J.M.; Vizcaino, S.: Tribological study of NiCrBSi coating obtained by different processes. *Tribol. Int.* **36**(3), 181–187 (2003)
40. Luo, X.; Tang, R.; Long, C.; Miao, Z.; Peng, Q.; Li, C.: Corrosion behavior of austenitic and ferritic steels in supercritical water. *Nucl. Eng. Technol.* **40**(2), 147–154 (2008)
41. Loto, R.T.: Study of the corrosion behaviour of S32101 duplex and 410 martensitic stainless steel for application in oil refinery distillation systems. *J. Market. Res.* **6**(3), 203–212 (2017)
42. Gutzeit J.: Effect of organic chloride contamination of crude oil on refinery corrosion. In: *CORROSION 2000. OnePetro* (2000)
43. Marcus, P.; Maurice, V.; Strehblow, H.H.: Localized corrosion (pitting): a model of passivity breakdown including the role of the oxide layer nanostructure. *Corros. Sci.* **50**(9), 2698–2704 (2008)
44. Moghaddasi, M.; Bozorg, M.; Aghaie, E.; Bakhtiyari, H.; Torbati-Sarraf, H.: Corrosion and wear analysis of high-velocity oxy-fuel sprayed WC-10Co-4Cr and colmonoy-6 coatings on nickel-aluminum bronze alloy substrate. *J. Mater. Eng. Perform.* **30**(10), 7564–7576 (2021)
45. Mele, C.; Lionetto, F.; Bozzini, B.: An erosion-corrosion investigation of coated steel for applications in the oil and gas field, based on bipolar electrochemistry. *Coatings* **10**(2), 92 (2020)
46. Guo, L.; Zheng, H.; Liu, S.; Li, Y.; Feng, C.; Xu, X.: Effect of heat treatment temperatures on microstructure and corrosion properties of Inconel 625 weld overlay deposited by PTIG. *Int. J. Electrochem. Sci.* **11**(7), 5507–5519 (2016)
47. Rustandi, A.; Sirait, G.; Saputra, A.; Sadeli, Y.: The use of electrochemical impedance spectroscopy method for corrosion resistance evaluation of 2205 and 410s stainless steels in aqueous sodium chloride solution. In: *IOP Conference Series: Materials Science and Engineering*, vol. 299, no. 1, p. 012053. IOP Publishin (2018)
48. Li, D.; Guruvenket, S.; Hassani, S.; Bousser, E.; Azzi, M.; Szpunar, J.A.; Klemberg-Sapieha, J.E.: Effect of Cr interlayer on the adhesion and corrosion enhancement of nanocomposite TiN-based coatings deposited on stainless steel 410. *Thin Solid Films* **519**(10), 3128–3134 (2011)
49. Chandran, S.; Vinayak, S.N.; Subramanian, V.; Rangarajan, S.; Velmurugan, S.; Narasimhan, S.V.; Ramasubbu, V.; Albert, S.K.: Effect of substrate dilution on corrosion of colmonoy-6 weld overlays in nitric acid. *Int. J. Nucl. Energy Sci. Technol.* **6**(3), 199–212 (2011)
50. Ding, Y.P.; Liu, R.; Wang, L.; Li, J.H.; Yao, J.H.: Corrosion and wear performance of stellite alloy hardfacing prepared via laser cladding. *Prot. Met. Phys. Chem. Surf.* **56**, 392–404 (2020)
51. Kim, H.G.; Ahn, S.H.; Kim, J.G.; Park, S.J.; Lee, K.R.: Electrochemical behavior of diamond-like carbon films for biomedical applications. *Thin Solid Films* **475**(1–2), 291–297 (2005)
52. Zeng, Q.; Sun, J.; Emori, W.; Jiang, S.L.: Corrosion behavior of thermally sprayed NiCrBSi coating on 16MnR low-alloy steel in KOH solution. *J. Mater. Eng. Perform.* **25**(5), 1773–1780 (2016)
53. Li, L.; Liu, X.Y.; Wang, X.; Wu, M.: Effect of cooling methods on mechanical and corrosion properties of Inconel 625 during solution treatment. In: *Journal of Physics: Conference Series*, vol. 1948, no. 1, p. 012127. IOP Publishing, (2021)
54. Sajjad, U.; Abbas, A.; Sadeghianjahromi, A.; Abbas, N.; Liaw, J.S.; Wang, C.C.: Enhancing corrosion resistance of Al 5050 alloy based on surface roughness and its fabrication methods; an experimental investigation. *J. Market. Res.* **1**(11), 1859–1867 (2021)
55. Hagen, C.M.; Hognestad, A.; Knudsen, O.Ø.; Sørby, K.: The effect of surface roughness on corrosion resistance of machined and epoxy coated steel. *Prog. Org. Coat.* **1**(130), 17–23 (2019)
56. Zheng, S.; Cai, Z.; Pu, J.; Zeng, C.; Wang, L.: Passivation behavior of VAlTiCrSi amorphous high-entropy alloy film with a high corrosion-resistance in artificial sea water. *Appl. Surf. Sci.* **542**, 148520 (2021)



57. Aladesanmi, V.I.; Fatoba, O.S.; Akinlabi, E.T.; Ikumapayi, O.M.: Analysis of wear properties and surface roughness of laser additive manufactured (LAM) Ti and TiB₂ metal matrix composite. *Mater. Today Proc.* **1**(44), 1279–1285 (2021)
58. Hady, H.; Hammood, A.S.; Thair, L.: The role of surface roughness during fretting corrosion of 316L stainless steel. *Mater. Today Proc.* **1**(42), 2326–2333 (2021)